PHYSICS OF FLUIDS VOLUME 12, NUMBER 5 MAY 2000

Nonlinear geostrophic adjustment, cyclone/anticyclone asymmetry, and potential vorticity rearrangement

Allen C. Kuo and Lorenzo M. Polvani
Department of Applied Physics and Applied Mathematics, Columbia University, New York, New York 10027

(Received 28 July 1999; accepted 30 December 1999)

Within the context of the rotating shallow water equations, it is shown how initially unbalanced states possessing certain symmetries dynamically evolve to lose those symmetries during nonlinear geostrophic adjustment. Using conservation law methods, it is demonstrated that the adjustment of equal and opposite (circular) mass imbalances results in a balanced end state where cyclones are stronger than anticyclones; the reverse holds true for momentum imbalances. In both cases, the degree of this asymmetry is shown to be directly proportional to the amount of initial imbalance (a measure of the nonlinearity occurring during time-dependent adjustment). On the other hand, the degree of asymmetry is maximal for imbalances of Rossby deformation scale. As for the potential vorticity, it is shown that its final profile can be noticeably different from its initial one; from an Eulerian perspective, this rearrangement is not confined to uniform shifts of potential vorticity fronts. Direct 2D numerical initial value problems confirm the asymmetry in the predicted final states and establish a relatively fast time scale for adjustment to complete. The robustness of these results is confirmed by studying, in addition, the adjustment of elliptical mass imbalances. The numerical integrations reveal that, during geostrophic adjustment, potential vorticity rearrangement occurs irreversibly on a fast wave time scale. © *2000 American Institute of Physics.*
[S1070-6631(00)02204-2]

I. INTRODUCTION

Geostrophic adjustment is the process by which a rotating fluid in an initially unbalanced ageostrophic state evolves toward a state of increasing balance. Rossby,[1] in a celebrated article, set an analytical framework for finding this final balanced state given an initially unbalanced flow. A large body of work on this subject followed, e.g., Refs. 2–8 among many (see Kuo[9] for an extensive review of the literature). In this article, we show that the nonlinear geostrophic adjustment of unbalanced mass and momentum fields constitutes a purely dynamical symmetry breaking process, whereby ‘‘symmetric’’ (to be clarified below) initial conditions become asymmetric in time.

In a variety of settings, there is observational evidence for asymmetries in the number, size, and strength of cyclonic and anticyclonic vortices: in the oceanic mesoscale[10] (anticyclonic favored), in the tropospheric midlatitudes[11] (cyclonic favored), in the Jovian atmosphere[12] (anticyclonic favored), in numerical experiments of freely evolving shallow water turbulence[13,14] (anticyclonic favored), and 3D balanced turbulence[15] (anticyclonic favored). A causal explanation for such asymmetries is likely to be highly dependent on the specific circumstances themselves, and hence we do not expect a single explanation to be universally applicable. However, since geostrophic adjustment is constantly at work in the atmospheres and oceans, understanding how asymmetry arises during adjustment may lead to a better understanding of at least one factor in observed cyclone/anticyclone asymmetries. In this article, we consider the simplest physical model that is capable of capturing the asymmetry: the rotating shallow water equations.

Specifically it is shown here that equivalent magnitude positive and negative unbalanced pressure perturbations (i.e., initially symmetric about a mean) adjust in such a way that the pressure fields are no longer symmetric at the balanced end states. The same result is shown to hold for the adjustment of equivalent magnitude, but opposite in parity, velocity fields. While the existence of such asymmetries in the final states is hardly surprising, given the nonlinear nature of the equations, it seems to have been largely ignored in previous studies of the adjustment problem. For instance, one might like to know whether the cyclones that emerge from the adjustment of an unbalanced pressure low are stronger or weaker than the anticyclones that emerge from a corresponding unbalanced pressure high. The purpose of the present article, therefore, is to study this asymmetry as a function of the two key parameters of the problem. The first is the amount of *initial imbalance*, which can also be understood as the degree of nonlinearity present during the time-dependent adjustment process. The second is the *spatial scale* of the initially unbalanced fields.

In both cases, the asymmetry is found to monotonically increase with the initial imbalance. This is to be expected, since decreasing the amount of imbalance leads to the quasigeostrophic regime, which displays no cyclone/anticyclone asymmetry.[16] The dependence of the asymmetry on the initial scale of the unbalanced fields, on the other hand, is nonmonotonic. It is small when the initial spatial scale is small, and generally increases to a relative maximum when the initial spatial scale becomes comparable to the Rossby deformation radius. Further increases in the initial length scale reduce the asymmetry gradually to a constant value.

Finally, in this article we bring to the fore another aspect of the geostrophic adjustment problem that seems to have been obscured in previous studies by the almost universal use of piecewise uniform initial conditions: the rearrangement of potential vorticity that occurs during geostrophic adjustment. We quantify the magnitude and form of such rearrangement and show that it can be substantial, even for parametric regimes that are not highly ageostrophic.

The article is divided into six sections. In Sec. II we examine the asymmetry which arises in the adjustment of an initially axisymmetric *mass* imbalance, and in Sec. III we deal with the corresponding asymmetry for an initial *momentum* imbalance. In both cases, we compute the amount of energy that is lost to inertia–gravity waves during adjustment and the efficiency of such wave emission. Perhaps surprisingly, we will show that the mass and momentum cases lead to opposite conclusions regarding gravity wave emission and cyclone/anticyclone asymmetry. In Sec. IV, we discuss and quantify the change in potential vorticity between the initial and final states as a result of rearrangement during adjustment. To validate the results of Secs. II and III, and to explore nonaxisymmetric adjustment scenarios (which are beyond the reach of Lagrangian conservation law approaches),[1] 2D time-dependent initial-value adjustment calculations are presented in Sec. V, where we consider both axisymmetric and elliptical initial mass imbalances. In the elliptical case, we also show how the potential vorticity is rearranged *in time*. This will provide a direct example of how fast gravity waves, created during adjustment, may interact with and modify the slow potential vorticity dynamics. The implications of this last result are discussed in Sec. VI.

II. MASS ADJUSTMENT

Consider a one-layer fluid obeying the rotating shallow water equations.[17] Following Rossby,[1] we use a Lagrangian formulation and, for simplicity, we treat purely axisymmetric problems first (the more complicated elliptical case is treated in Sec. V). The nondimensional equations which relate the initial (subscript ''0'') unbalanced initial states to the final (no subscript) balanced end states are

$$rv+\frac{r^2}{2}=r_0v_0+\frac{r_0^2}{2}, \tag{1}$$

$$(1+\eta)r\frac{dr}{dr_0}=(1+\eta_0)r_0, \tag{2}$$

where v denotes the azimuthal component of the velocity, r the radial position of Lagrangian fluid elements, and η represents the deviation of the free surface of the fluid from a (dimensional) mean height H. The nondimensionalization used here is as follows:

$$\begin{aligned} v^* &= (\sqrt{gH})v, \\ h^* &= H(1+\eta), \\ r^* &= L_d r, \end{aligned} \tag{3}$$

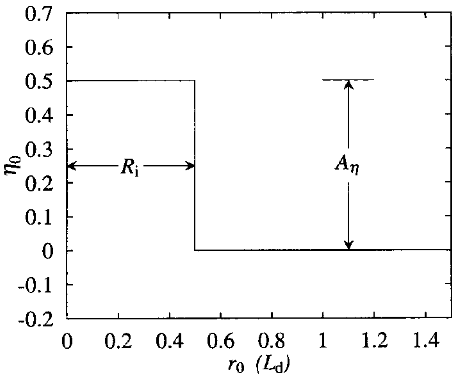

FIG. 1. Schematic of the unbalanced initial conditions for mass adjustment with an axisymmetric configuration. The parameters shown here are: $A_\eta=0.5$ and $R_i=0.5$.

where starred quantities are dimensional, and g is the gravitational acceleration, h^* is the full depth/height of the fluid, $L_d\equiv\sqrt{gH}/f$ is the Rossby deformation radius, and f is the constant Coriolis parameter (equal to twice the angular velocity of rotation). Note that η can also be interpreted as a pressure deviation from a mean and hence we will sometimes refer to it as such.

These two equations express the conservation of angular momentum and mass, respectively. Given the initial fields v_0 and η_0, the final fields v and η can be calculated if one assumes, in addition, that the final flow is balanced, i.e.,

$$\frac{d\eta}{dr}=v+\frac{v^2}{r}. \tag{4}$$

Combining (1), (2) and (4) one first obtains a single equation for $r_0(r)$ (cf. Ref. 18) which is then transformed into an equation for the final radial state coordinate $r(r_0)$,

$$\begin{aligned} &\frac{d^2r}{dr_0^2}+\left(\frac{dr}{dr_0}\right)^3\frac{1}{1+\eta_0}\left[\frac{r_0}{2}+v_0-\frac{r^2}{2r_0}+\frac{r_0}{r^2}\right. \\ &\quad\left.\times\left(\frac{r_0}{2}+v_0-\frac{r^2}{2r_0}\right)^2\right]-\left(\frac{dr}{dr_0}\right)\left(\frac{1}{r_0}+\frac{1}{1+\eta_0}\frac{d\eta_0}{dr_0}\right) \\ &\quad+\left(\frac{dr}{dr_0}\right)^2\frac{1}{r}=0. \end{aligned} \tag{5}$$

For simplicity we study the following pairs of initial conditions

$$\begin{aligned} &v_0(r_0)=0, \\ &\eta_0(r_0)=\begin{cases} \pm A_\eta & \text{for } 0<r_0<R_i, \\ 0 & \text{for } r_0>R_i, \end{cases} \end{aligned} \tag{6}$$

consisting of a fluid at rest with a positive (elevation) or negative (depression) top-hat height perturbation. Such initial conditions are illustrated in Fig. 1. The problem, as we have defined it, is thus governed by two parameters: A_η, the amplitude of the initial mass imbalance, and R_i, its initial radius. Our goal is to show that pairs of initial conditions that are initially symmetric about $\eta_0=0$ end up being asymmetric (about $\eta=0$) at the final state, and to quantify the dependence of this asymmetry on R_i and $|A_\eta|$.

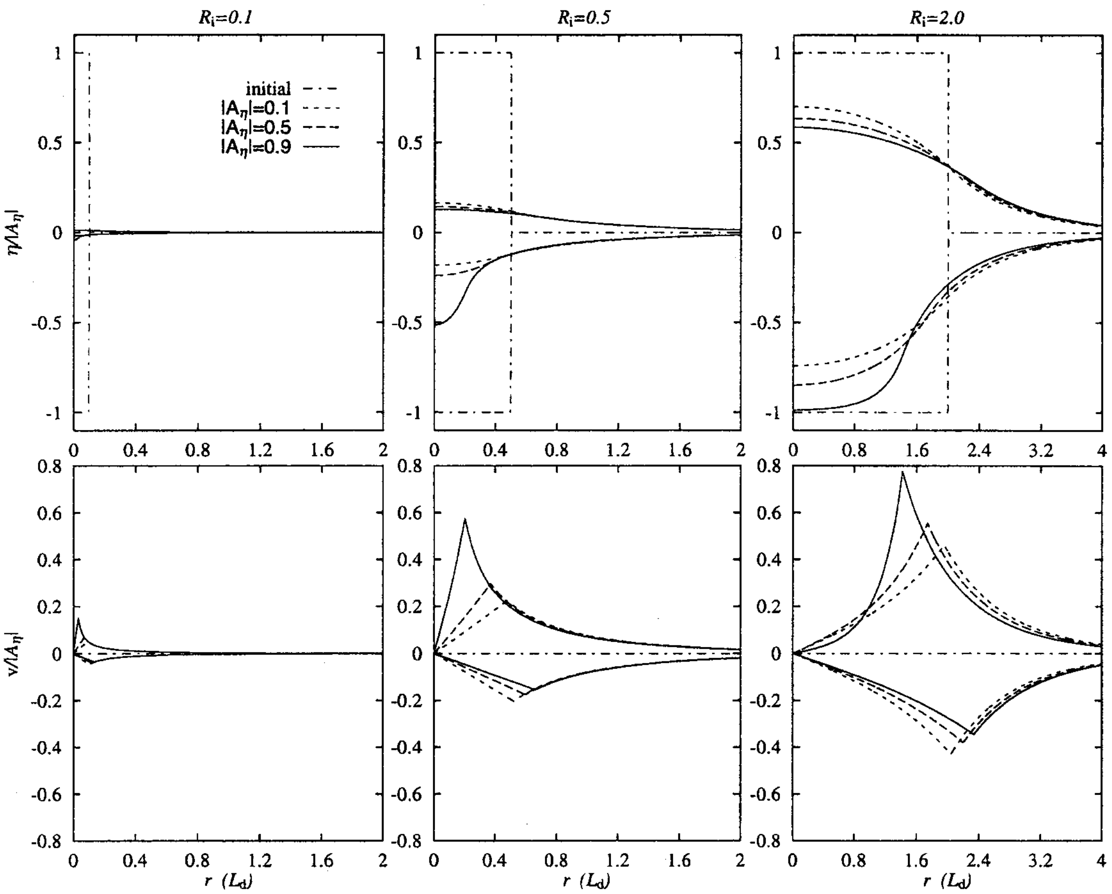

FIG. 2. Axisymmetric mass adjustment. The final state, balanced height and velocity fields. The dash-dotted lines show the initial conditions.

It is worth making a brief comment regarding our choice of initial conditions. One might object that the fluid height is not the proper initial field to choose. The potential vorticity Π, defined by

$$\Pi \equiv \frac{v_r+(v/r)+1}{1+\eta}, \tag{7}$$

is in many ways a more fundamental quantity, and thus one might be tempted to examine positive and negative potential vorticity anomalies $(\Pi-1)$ of equal amplitude.

Following that train of thought, consider taking the initial potential vorticity to be of the form

$$\Pi_0(r_0)-1=\begin{cases}\pm A_\Pi & \text{for } r_0<R_i,\\ 0 & \text{for } r_0>R_i,\end{cases}$$

and initializing the flow with $v_0=0$ and η_0 derived from the definition (7). The initial maximum in η_0 for A_Π could in that case be much smaller in magnitude than the corresponding maximum in η_0 for $-A_\Pi$. This large discrepancy in the initial height would surely lead to a much more violent adjustment for the initially negative potential vorticity anomaly. It would not be surprising, therefore, that the final states are asymmetric, but this would be a flagrant example of ''loading the dice.'' The key point is that potential vorticity is a poor quantity to use for specifying initial conditions here because, by itself, it cannot measure how far the flow deviates from geostrophic balance. This deviation, of course, is the essential parameter that controls the amount of adjustment and the asymmetry that develops in the end state.

Before presenting solutions, we briefly discuss how Eq. (5), with initial conditions (6), is solved numerically. The integration starts at a point $r_0=\delta$, $\delta\ll 1$, where the final Lagrangian displacements are known to be zero so that $r=0$ here. Slopes are guessed at this point and the integrations marched forward in r_0 until, at a point far away from the initial discontinuity (ten deformation radii), we require $r=0$ (within a numerical tolerance factor). This condition is simply the requirement that the Lagrangian displacements vanish far from the initial mass imbalance. The numerical solutions so obtained were also independently validated with an iterative (nonlinear) relaxation technique. Once $r(r_0)$ is obtained from (5), the final v and η are computed from (2) and (4).

In Fig. 2, we present the final adjusted fields η and v that are obtained from the above mentioned procedure. The solutions are plotted in three different columns, one for each representative choice of the radius of the initial imbalance: smaller than $(R_i=0.1)$, comparable to $(R_i=0.5)$ and greater than $(R_i=2.0)$ the deformation radius. The top row shows η and the bottom row shows the corresponding balanced velocity v. In each frame, the solutions for six values of the imbalance/nonlinearity parameter A_η are shown, three being

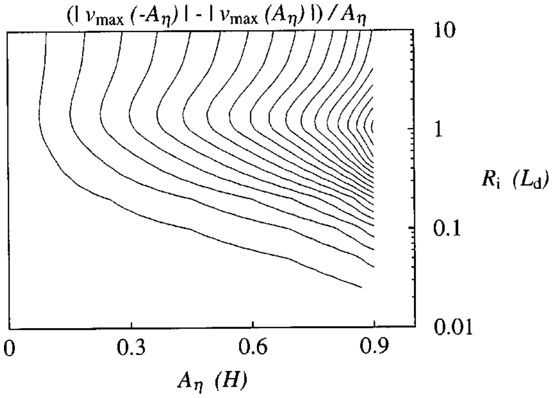

FIG. 3. Axisymmetric mass adjustment. The normalized difference, in the peak velocity at the final states, between unbalanced initial elevations and depressions. Contours start at 0.025 for small R_i and increase in intervals of 0.025.

unbalanced height elevations and three being the corresponding height depressions. The values of A_η are alse chosen to be representative of initial conditions with weak ($A_\eta = \pm 0.1$), medium ($A_\eta = \pm 0.5$), and strong ($A_\eta = \pm 0.9$) imbalance. For easy comparison, each plot shows the two symmetric initial conditions in dash-dotted lines. Note that, to make comparisons meaningful, all plotted solutions are scaled by $|A_\eta|$, and that the scale on the ordinate axis is identical across the three values of R_i.

The most prominent qualitative features in Fig. 2 are as follows. First, when R_i is small ($=0.1$) rotational effects are small and, in spite of the presence of centrifugal terms, the asymmetry is hard to detect. Second, for an initial imbalance comparable to the deformation radius ($R_i = 0.5$), it can be seen that the velocities associated with the initial height depressions are greater than those for the corresponding initial height elevations. Also, the velocity maximum shifts inwards for the former and outward for the latter. Third, for $R_i = 2.0$, the asymmetry is fully apparent in all of the fields. Notice again how the larger final velocities are associated with the initial depressions. In other words the cyclonic vortices that emerge from the adjustment of an initial surface depression are stronger than the anticyclones produced by an initial surface elevation of equal magnitude.

Qualitatively speaking, one might conclude from Fig. 2 that the asymmetry increases in all cases with $|A_\eta|$. It also appears that the asymmetry increases monotonically with R_i but, as we show next by examining the (A_η, R_i) parameter space more carefully, it turns out that this is not true: the relative asymmetry reaches a maximum near $R_i \approx 1$ and then tapers off to a constant. This is illustrated in Fig. 3, where the difference $|v_{\max}(-A_\eta)| - |v_{\max}(A_\eta)|$ (scaled by A_η) is contoured over the full (A_η, R_i) parameter space. This quantity measures the relative asymmetry between $\pm A_\eta$ initial states. From that figure it is clear that the maximum asymmetry occurs at a value of $R_i \approx 1$. Beyond that, the relative asymmetry decreases slightly and then saturates to a constant value.

In order to understand which balance of terms is dominant in the final steady-state vortex, the relative importance of the centrifugal and Coriolis terms needs to be considered.

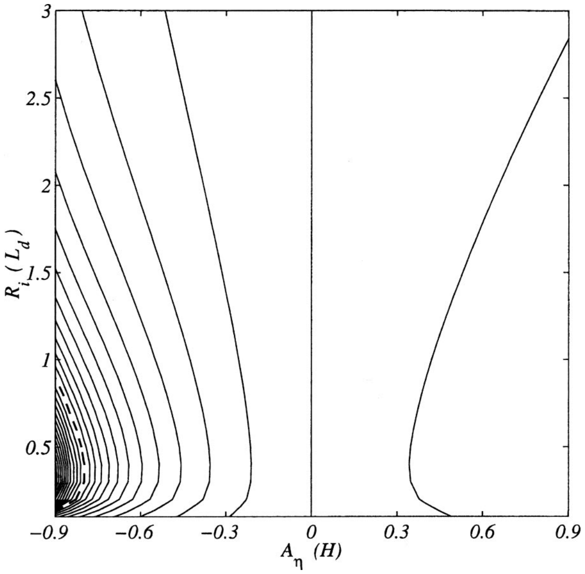

FIG. 4. Axisymmetric mass adjustment: contour plot of the ratio $\max[v^2/r]/\max[|v|]$ (where the maximum is taken over r), expressing the relative importance of the centrifugal effect to the Coriolis effect in the final steady-state vortex. The contours start at zero for $A_\eta = 0$ and increase away from this value in units of 0.25. The dashed line represents the contour for which $\max[v^2/r]/\max[|v|] = 1$.

We summarize this information in Fig. 4, where the ratio $\max[v^2/r]/\max[|v|]$ (where the maximum is taken over r) is contoured in the (A_η, R_i) parameter space. Though not evident in the plot, the contour lines become symmetric about $A_\eta = 0$ as $|A_\eta| \to 0$. This is the regime where the asymmetry disappears and the vortices are geostrophically balanced. Centrifugal dominance is indicated in the lower left corner of the diagram (negative A_η), below the dashed/unity contour (which indicates the gradient wind balance regime). For large amplitude initial depression, the centrifugal effect can be over four times stronger than the Coriolis effect. On the other hand, for the final state anticyclones (positive A_η), the ratio is always less than ≈ 0.2. Notice that this does not imply that centrifugal dominance is impossible in an anticyclone, but to create such a vortex from mass adjustment, the initial height perturbation would have to be greater than the ambient fluid depth.

Up to this point, we have been considering only the final balanced steady-state solutions and have ignored the complicated transient behavior which arises during adjustment. However, it is this transient behavior, involving the generation of gravity waves that carry energy away from the region of initial imbalance, that explains why the flow in the final state has less energy than it does initially.[8] Consideration of the final state energy thus allows one to quantify, albeit indirectly, the amount of gravity waves generated during the adjustment process.

A quantity traditionally associated with the energetics of the adjustment process is the ratio $|\Delta KE/\Delta PE|$, where the nondimensional kinetic and perturbation (or available) potential energies per unit area are defined by

$$KE \equiv \frac{1}{2}\int_0^\infty (1+\eta) v^2 r\, dr, \tag{8}$$

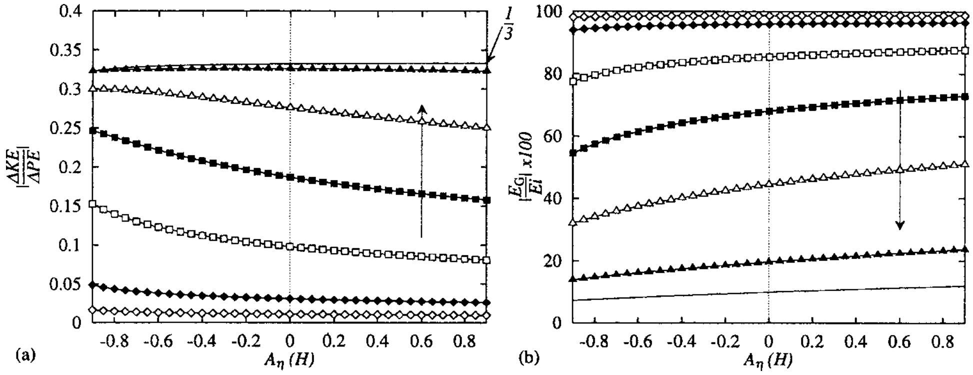

FIG. 5. (a) The ratio $|\Delta KE/\Delta PE|$ for the case of axisymmetric mass adjustment. The arrow points in the direction of increasing R_i and decreased efficiency at producing gravity waves. (b) Absolute energy change due to gravity waves emission normalized by the initial energy. The arrow points in the direction of increasing R_i. In (a) and (b), the values corresponding to the different symbols are: $R_i=0.1$, 0.2, 0.5, 1, 2, 5. The solid line corresponds to $R_i=10$.

$$PE\equiv\frac{1}{2}\int_0^\infty \eta^2 r dr, \tag{9}$$

and Δ denotes the change from the final state to the initial state. The relationship between this ratio and the energy loss due to the flux of gravity waves, $E_G\equiv\Delta E$ (where $E=KE+PE$), is

$$\frac{\Delta KE}{\Delta PE}=\frac{E_G}{\Delta PE}-1. \tag{10}$$

An increase in magnitude of this ratio corresponds to a decrease in the percentage of the initial available potential energy used to generate gravity waves. This ratio, therefore, is inversely proportional to the *efficiency* of gravity wave production, rather than being an absolute measure of gravity wave production.

Curves for $|\Delta KE/\Delta PE|$ vs. the imbalance parameter A_η are plotted, for several values of the initial radius R_i, in Fig. 5(a). First, one can see that initial depressions are less efficient generators of gravity waves than the corresponding initial elevations, since this ratio is a monotonically decreasing function of A_η for any given R_i. Second, it is clear that as the radius of the initial imbalance decreases, the efficiency of gravity wave generation increases. In the limit $R_i\rightarrow 0$, $E_G/\Delta PE=1$ so that all of the initial available potential energy is converted into gravity wave energy. This makes sense, since in the limit of no rotation, there is a maximum change in potential energy (the fluid column collapses entirely) while the initial and final kinetic energies are zero. Third, the maximum value of $|\Delta KE/\Delta PE|$ is 1/3, the same[18] as in the adjustment of a single initial height ''step.'' Recall that this 1/3 value must be recovered in the limit $R_i\rightarrow\infty$ and is related to the least efficient gravity wave generation scenario, occurring when $E_G/\Delta PE=2/3$.

While $|\Delta KE/\Delta PE|$ measures the efficiency of gravity wave generation, i.e., what fraction of the initial available potential energy is used in the generation of gravity waves, one might ask a more basic question: which initial configuration (depression or elevation) generates *more* gravity waves? To answer this, we plot in Fig. 5(b) a more absolute measure of gravity wave generation, i.e., $|E_f-E_i|/E_i=E_G/E_i$, where the subscripts i and f refer to initial and final states. From Fig. 5(b) one can immediately read off the percentage of the initial energy that gets converted to gravity waves for different values of R_i. For instance, for an initial mass imbalance with $R_i=1$, roughly 60% of the initial energy is lost to gravity waves.

Figure 5(b) shows that, for given R_i and $|A_\eta|$, the initial height elevations are always associated with greater absolute loss of energy than initial height depressions (recall that both have the same E_i initially). This may be taken as an indication that initial height elevations are associated with more gravity wave emission or ''activity.'' The discrepancy in E_G between elevations and depressions is greatest around $R_i=1.0$, as seen in the figure. This reinforces our previous finding that the deformation radius is the preferred initial length scale for asymmetry.

III. MOMENTUM ADJUSTMENT

Having determined the key properties of the adjustment of an initial *mass* imbalance, we now consider the complimentary problem, namely the adjustment of an initial *momentum* imbalance. To do this, we take the unbalanced initial conditions to be

$$v_0(r_0)=\begin{cases} A_v(r_0/R_i) & \text{for } r_0<R_i, \\ A_v(R_i/r_0)^2 & \text{for } r_0>R_i, \end{cases}$$
$$\eta_0(r_0)=0, \tag{11}$$

as illustrated in Fig. 6. The two parameters in the case are A_v, the amplitude of the initially unbalanced velocity and, as in the previous section, the radius R_i of the (velocity maximum of the) initial imbalance. Note that the fall off rate of the velocity fields at large r is chosen to be proportional to $(1/r^2)$. This is the simplest algebraic fall off rate that allows the initial conditions to have a finite amount of energy (a $1/r$ fall off rate does not).

The final state balanced fields η and v resulting from the numerical solution of (5) with initial conditions (11) are shown in Fig. 7. As in previous sections, we illustrate the key qualitative results with three choices of the initial radius R_i, corresponding to diameters less than, equal to, and greater than the deformation radius, and six choices of the

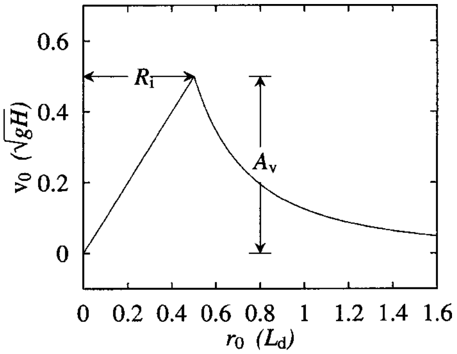

FIG. 6. Schematic of the initially unbalanced velocity field, axisymmetric configuration, with amplitude parameter $A_v = 0.5$ and radius $R_i = 0.5$. The corresponding initial height field is flat.

initial velocity imbalance A_v, three (weak, medium, strong) for initially unbalanced cyclones and three for the corresponding anticyclones. For each of the three cases of R_i, the most prominent qualitative features in Fig. 7 are noted below.

When R_i is small (=0.1), the velocity field barely adjusts, and its symmetry is thus very nearly retained between $\pm A_v$ states. Such behavior is to be expected in this case, since the rotational influence is small. However, the balanced perturbation height fields corresponding to these nearly symmetric velocity distributions are in fact strongly asymmetric: both cyclonic and anticyclonic initial states lead to height depressions (except in the case $A_v = -0.1$). The cases where $A_v < 0$ are examples of ''anomalous lows,'' where anticyclones are associated with low (rather than high) pressure.[19] Their existence implies that the dominant balance is cyclostrophic when R_i is small.

For the midrange value, $R_i = 0.5$, the velocity in the cyclonic cases tends to adjust more than in the anticyclonic cases. An outward shift is apparent when $A_v > 0$, whereas the inward shift is barely detectable when $A_v < 0$. In the latter, it is the height field that again mostly adjusts to the velocity field. In addition, the centrifugal terms are not as dominant as in the $R_i = 0.1$ case: notice that the anomalous low appears only at large negative initial velocity ($A_v = -0.9$).

When $R_i = 2.0$, we see that both cyclonic and anticyclonic velocities show adjustment. The outward (inward) shift in the cyclonic (anticyclonic) case indicates Coriolis deflection, and thus indicates geostrophic (rather than cyclostrophic) control of the adjustment. As expected in this geostrophic regime, the cyclonic (anticyclonic) velocities are associated with pressure lows (highs). In general, the anticyclonic cases have larger maximum velocities and stronger pressure perturbations at the final state than the cyclonic ones for given $|A_v|$.

In Fig. 8 we again bring out the asymmetry by plotting the difference in the final $v_{\max}$ between $\pm A_v$ initial states. Just as in the case of mass adjustment, it can be seen that the asymmetry increases with the initial imbalance $|A_v|$, and that

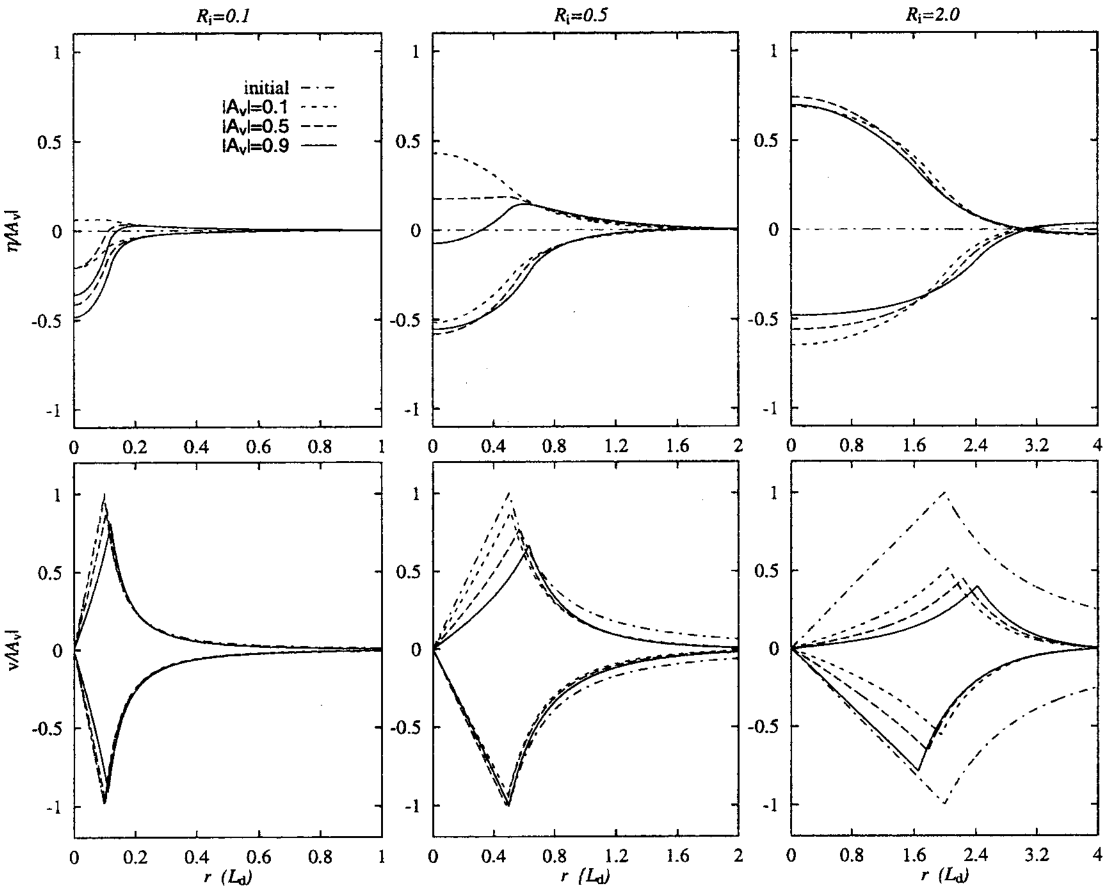

FIG. 7. Axisymmetric momentum adjustment. The final state, balanced height, and velocity fields. The dash-dotted lines show the initial conditions.

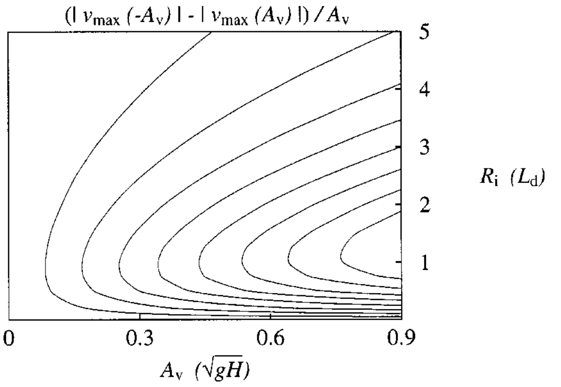

FIG. 8. Axisymmetric momentum adjustment. The normalized difference, in the peak velocity at the final states, between unbalanced initial cyclones and anticyclones. Contours start at 0.05 for small R_i and increase in intervals of 0.05.

the maximum asymmetry (for a given A_v) is found around $R_i \approx 1$.

In this case too, it is useful to consider how the ratio $\max[v^2/r]/\max[|v|]$, plotted in Fig. 9, varies in the parameter space. Roughly speaking, two main regions can be identified in that plot, and they are separated by the dashed line corresponding to $\max[v^2/r]=\max[|v|$. Above the dashed line the balance is geostrophic and below it the balance is cyclostrophic (as $R_i \rightarrow 0$). It is important to note, however, that the transition from one regime to the other is quite different depending on the sign of A_v. On the left side of the figure ($A_v<0$) the dashed line corresponds to inertial balance, where the Coriolis force balances the centrifugal force [i.e., they are of similar magnitude but opposite sign. See (4)], and the height field is nearly flat. In contrast, the dashed line on the right side of the figure ($A_v>0$) corresponds to gradient wind balance, where the centrifugal, Coriolis, and pressure gradient forces are all of comparable magnitude [and of like sign in (4)].

Finally, we examine the energetics. In Fig. 10(a) we plot the ratio $|\Delta PE/\Delta KE|$ (rather than $|\Delta KE/\Delta PE|$) since, unlike mass adjustment, only kinetic energy is initially present. Again, this ratio is inversely proportional to the efficiency of production of gravity waves. The key result here is that the nature of the energetics is very different from that associated with axisymmetric mass adjustment (cf. Fig. 5). Notice three main points.

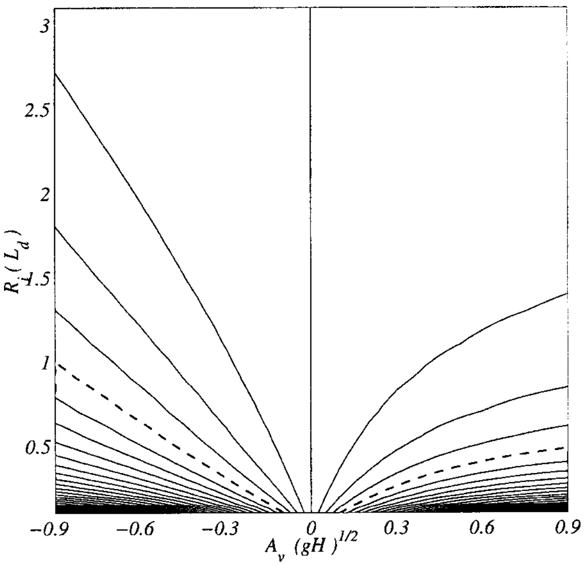

FIG. 9. Axisymmetric momentum adjustment: contour plot of the ratio $\max[v^2/r]/\max[|v|]$ (where the maximum is taken over r), expressing the relative importance of the centrifugal effect to the Coriolis effect in the final steady-state vortex. The contours start at zero for $A_v=0$ and increase away from zero in intervals of 0.25. The dashed lines represent the contours for which $\max[v^2/r]/\max[|v|]=1$.

First, as the initial spatial scale R_i decreases $|\Delta PE/\Delta KE|$ increases, implying less efficiency at producing gravity waves (this result was obtained by Schubert *et al.*[20] using linear arguments). Recall that the opposite effect was found for mass adjustment—less efficiency was associated with *large* spatial scales. These results follow from the simple physical fact that the velocity field does not adjust much in the small R_i weak rotation limit, whereas an initial top-hat mass imbalance must totally collapse under gravity in this limit.

Second, unlike the case of mass adjustment, the value of R_i determines whether positive or negative A_v initial states are more efficient at producing gravity waves. When $R_i \gtrsim 2$,

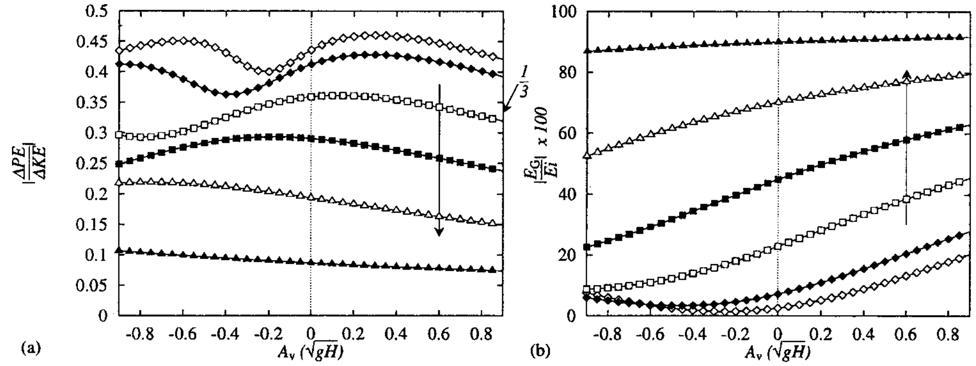

FIG. 10. (a) The ratio $|\Delta PE/\Delta KE|$ plotted here for the case of unbalanced, axisymmetric momentum adjustment. The arrow points in the direction of increasing R_i and increasing efficiency at producing gravity waves. (b) Absolute energy change due to gravity waves emission normalized by the initial energy. The arrow points in the direction of increasing R_i. In both (a) and (b), the values corresponding to the different symbols are: $R_i=0.1$, 0.2, 0.5, 1, 2, 5.

cyclonic initial states states are more efficient than the corresponding anticyclonic initial states. When $R_i \lesssim 2$, the efficiency depends on the value of $|A_v|$ for fixed R_i.

Third, it is not clear that a most inefficient gravity wave generation case exists in the $R_i \to 0$ limit. Recall that, in contrast, for mass adjustment the most inefficient gravity wave generation scenario is associated with the ratio $\Delta KE/\Delta PE = 1/3$. There seems to be no convergence to a corresponding limiting ratio for the $R_i \ll 1$ curves in Fig. 10(a).

In Fig. 10(b), we plot E_G/E_i. In general, larger R_i is associated with stronger gravity wave production, also in contrast to the case of mass adjustment. Notice that for $R_i \gtrsim 0.5$, the $A_v > 0$ states produce more gravity waves than the $A_v < 0$ states, while for $R_i \lesssim 0.5$ the amount of gravity wave energy flux reaches a local minimum for some $A_v < 0$. This occurs when the adjustment in the height and velocity fields is minimal, and corresponds to the dashed lines in the lower left corner region in Fig. 9, where the Coriolis force is initially to a large extent in balance with the centrifugal force.

IV. POTENTIAL VORTICITY REARRANGEMENT

The thoughtful reader will have noticed that we have made little reference to potential vorticity in the above discussions of mass and momentum adjustment. As already mentioned, potential vorticity by itself is a not a good measure of balance. Its evolution under adjustment, however, is worth considering in some detail. Recall first that potential vorticity is materially conserved in nondissipative shallow water flows such as those we have been discussing in the previous sections. This does not imply, of course, that the potential vorticity field cannot change from its initial distribution (when viewed in an Eulerian framework). The purpose of this section is to illustrate and quantify a simple fact that seems to have been little emphasized in previous studies of adjustment, namely, that the potential vorticity, after adjustment has completed, can be very different from its initial configuration. The time-dependent aspect of potential vorticity rearrangement and its implications for the notion of balance are discussed in Sec. V B below.

In earlier studies, the only potential vorticity changes that have been calculated in the context of nonlinear geostrophic adjustment have been advective shifts, mainly because analytical tractability dictates the use of piecewise constant potential vorticity. Advective shifts of the jumps bounding regions of uniform potential vorticity uniform are, in an Eulerian perspective, the only possible outcome of adjustment (given material conservation). A notable exception is found in McWilliams.[21] His Fig. 2 is, as far as we can tell, the first clear demonstration in an Eulerian framework that, when the initial potential vorticity distribution is nonuniform, geostrophic adjustment results in potential vorticity rearrangement that is richer than a simple uniform shift (Blumen[6] considered lowest-order nonlinear corrections to geostrophic adjustment using nonpiecewise constant potential vorticity, but did not explicitly show the final potential vorticity fields).

In this section, we quantify the potential vorticity rearrangement that occurs during the geostrophic adjustment of an initially nonpiecewise uniform potential vorticity distribution, and we specifically show how final state cyclones and anticyclones differ in their potential vorticity profiles. For brevity, we limit ourselves to the cases of mass adjustment and initialize the fluid with no velocity and a height field given by

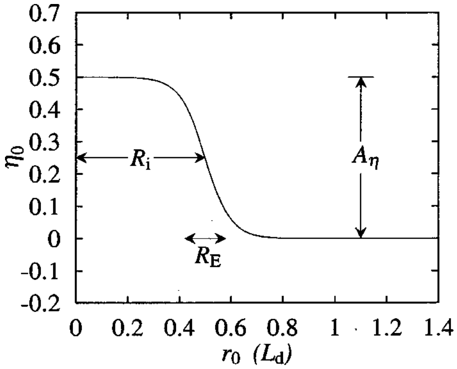

FIG. 11. Schematic of the initially unbalanced smooth-edged height field. The amplitude is $A_\eta = 0.5$, the radius $R_i = 0.5$, and edge width $R_E = 0.1$.

$$\eta_0(r_0) = 1 + \frac{A_\eta}{2}\left(1 - \tanh\left[\frac{(r_0 - R_i)}{R_E}\right]\right), \tag{12}$$

where $r_0 = \sqrt{(\sqrt{\lambda}x_0)^2 + (y_0/\sqrt{\lambda})^2}$ and λ, the aspect ratio, is set to unity ($\lambda \neq 1$ cases are discussed in the next section). These unbalanced top-hat-like axisymmetric initial conditions, depicted in Fig. 11, have smooth edges. The smoothness is controlled by the new parameter R_E, and the cases considered in Sec. II correspond to the limiting value $R_E \to 0$. As already mentioned, the reason for introducing the new parameter is that nonpiecewise-uniform initial potential vorticity distributions are needed in order to observe a potential vorticity rearrangement that is more than a mere uniform shift, in an Eulerian framework (recall that, in a Lagrangian framework, the shift is nonuniform for *any* initial potential vorticity profile). For the present purposes, it will suffice to examine a single case of R_E; $R_E = 0.1$ is chosen here.

In Fig. 12 we plot the initial and final perturbation potential vorticity fields associated with the mass adjustment of the fields in Eq. (12). Three cases are shown, corresponding to $R_i = 0.2$, 0.5, and 2.0. The egregious value $A_\eta = \pm 0.9$ is chosen to better illustrate the main qualitative results which hold throughout the entire (A_η, R_i) parameter space.

The potential vorticity rearrangement that accompanies nonlinear geostrophic adjustment is clearly seen in Fig. 12. As expected, the potential vorticity distribution expands (due to nonlinear advection) when $A_\eta > 0$ and contracts when $A_\eta < 0$. In the limit $R_E \to 0$, when the potential vorticity is discontinuous, the only noticeable result of the adjustment is a shift of the infinitely steep edges.[18] The finite R_E case clearly shows, however, that the adjustment of nonpiecewise uniform potential vorticity distributions results in more than a simple shift of the potential vorticity field. The most telling case is $R_i = 0.2$ in Fig. 12(b): the edges of the final potential vorticity are noticeably steeper than the initial ones.

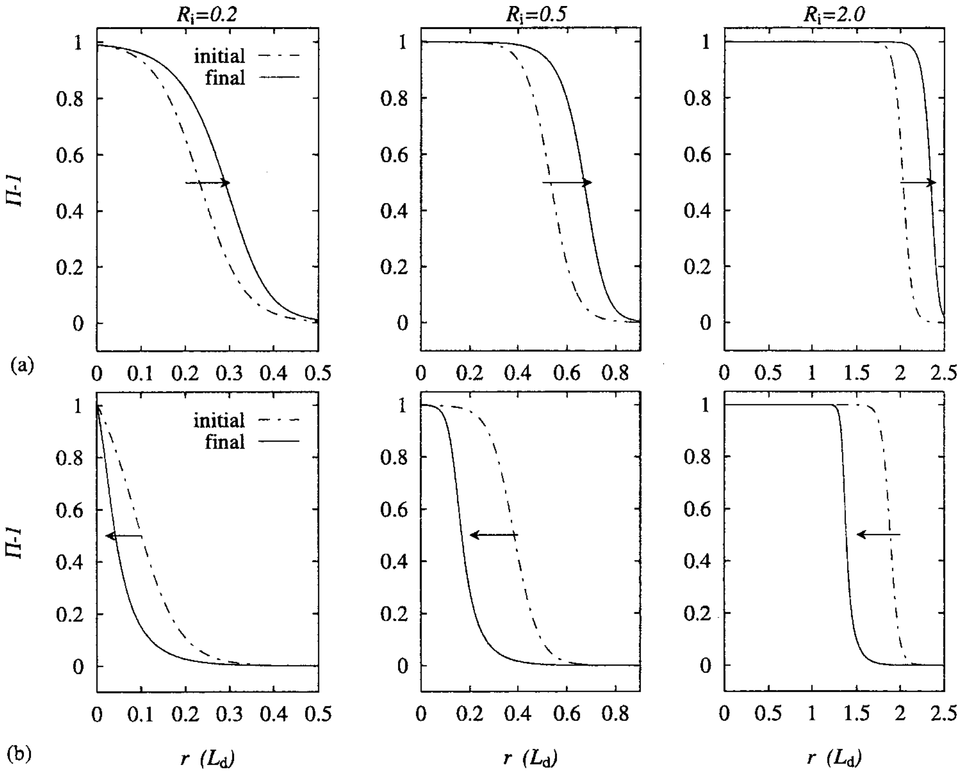

FIG. 12. The rearrangement of potential vorticity Π during axisymmetric mass adjustment. (a) $A_\eta=0.9$, (b) $A_\eta=-0.9$. In all cases $R_E=0.1$, and $\Pi-1$ is normalized so that the maximum value is 1.

In Fig. 13, we quantify the potential vorticity rearrangement over a larger portion of parameter space. In that figure we plot the relative change in the area $a(t)$ under the perturbation potential vorticity curve from the initial to the final state i.e., $|a(t=\infty)-a(t=0)|/a(t=0)$, where

$$a(t)\equiv\int_0^\infty|\Pi(r,t)-1|r\,dr. \qquad (13)$$

Notice that: (a) the contours are symmetric about $A_\eta=0$ when $|A_\eta|$ is small, but as $|A_\eta|$ increases, the symmetry is lost; (b) for given R_i and $|A_\eta|$, greater relative change is associated with height depressions (the left-hand side of the diagram); (c) for any A_η, a maximum relative change occurs around $R_i=0.5$, corresponding to final state vortices roughly one deformation radius in diameter; (d) the relative change in potential vorticity is not necessarily small. For instance, if A_η were taken to be a measure of the strength of the advective terms in the shallow water equations with a scaling similar to Gill's,[8] then A_η could be interpreted as an advective Rossby number. In that case, for an initial unbalanced height depression one deformation radius in diameter ($R_i=0.5$), 20% changes in the potential vorticity occur for Rossby numbers around 0.3.

V. 2D TIME-DEPENDENT COMPUTATIONS

In this section, numerical time-integrations of the shallow water equations are performed to verify that the end states predicted by conservation law methods (as in previous sections) are actually realized in practice. As McWilliams[21] has pointed out, using such methods, ''...there is no certainty *a priori* of the existence of a solution of the type sought... Nor is there any certainty of uniqueness in the adjusted state... even if a unique solution exists, there may not be an evolutionary pathway to it.'' In addition, the numerical integrations allow for a direct observation of the asymmetry which develops in time and provide information about the time required for adjustment to complete. Most importantly, the numerical method permits investigation of adjustment scenarios that are not amenable to analytic/conservation

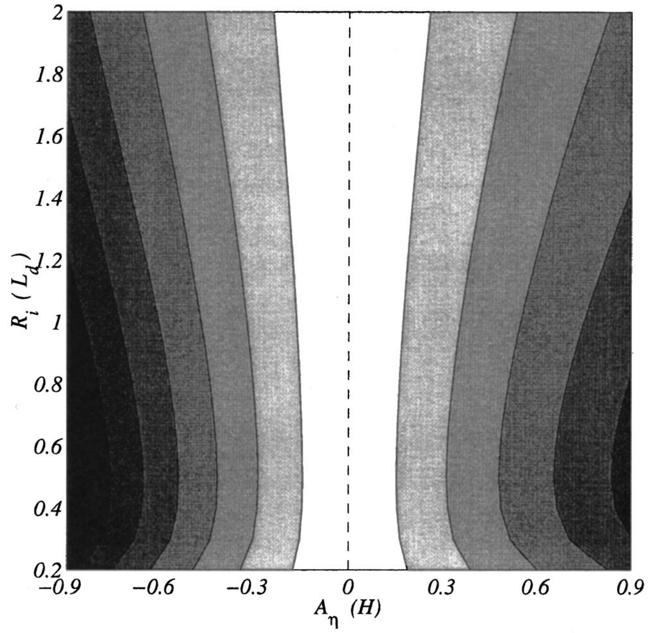

FIG. 13. Percent change in the initial potential vorticity anomaly during mass adjustment. The dashed line represents the zero contour; contours increase away from this line in intervals of 10%. For this parameter range, the percent change ranges from 0% to 70%.

methods, e.g., nonaxisymmetric unbalanced initial conditions where an asymptotic time-independent end state may not exist. In this latter case, the potential vorticity dynamics is considerably richer than the axisymmetric counterpart and will be discussed in some detail. For the sake of brevity, we limit ourselves to the study of initial mass imbalances here, and remark that the time-dependent adjustment of initial momentum imbalances has previously been studied (albeit in the cyclostrophic limit) by Lelong and McWilliams.[22]

Before presenting results in the next subsection, we remind the reader that the rotating shallow water equations admit shock solutions.[23] To accurately capture the time-dependent behavior of these equations, it is therefore necessary to use a numerical method that will allow such shocks to form. A fully two-dimensional weighted essentially nonoscillatory (WENO) shock-capturing code is employed here to solve the nondimensional shallow water equations, with time scaled by $(1/f)$, and velocity, horizontal distance, and fluid depth scaled as in (3). This method utilizes fully explicit fourth-order Runge Kutta time stepping, and is fifth-order accurate in space in smooth regions of the flow, and third-order accurate near discontinuities. We refer the reader to Jiang and Shu[24] for a description, and some test cases, of this numerical method. In the numerical results presented below, the computational domain is taken to be $x \in [-10,10]$ and $y \in [-10,10]$. For short time integrations $(t<20)$, the grid was taken to be 500×500, while long time results $(20<t<100)$ are obtained with a 400×400 grid. Sommerfeld outflow boundary conditions[25] are employed at the edges of the computational domain.

A. Axisymmetric mass adjustment

In Fig. 14, we plot the perturbation height field η resulting from the adjustment of an axisymmetric initial mass imbalance, with the initial height field given by (12) with $\lambda=1$ and the initial velocities identically zero. We have selected an initial imbalance with a moderate amplitude $|A_\eta|=0.5$, and with a size on the deformation scale $R_i=1.0$ (with edge width $R_E=0.1$). The left column illustrates the evolution of an initial elevation while the right column shows that of the corresponding depression (plotted upside down for easy comparison). For reference, the dotted line shows the end state computed using conservation methods. Recall that the numerical integrations are *fully* two-dimensional; because circular symmetry is retained throughout the computation, only a cross section of the height field is plotted. Three main points should be noted.

First, there is noticeable asymmetry in the form of the gravity waves that emanate from the unbalanced mass fields. The leading wave created by the adjusting elevation is a decaying shock (see $t=3$), while in the case of the depression it is a rarefaction wave (keep in mind that η has been inverted here). Later in time, at $t=6$, a shock forms behind this rarefaction and begins to overtake it; in the case of the elevation a secondary shock forms behind the leading one.

Second, the adjustment proceeds quite rapidly, and hence the asymmetry in the final states emerges relatively early. At $t=15$, the fields have very nearly settled into their asymptotic state. This should be contrasted with the 1D rectilinear case where the adjustment can in some instances take much longer to complete.[23] The adjustment time does, of course, depend on the type of initial imbalance (mass or momentum), its form, and its scale. However, from the theoretical work of Obukhov[3] and Blumen[7] it is known that, in general, flows in two spatial dimensions adjust at a faster rate than in one dimension. Our time-dependent numerical calculations are consistent with those theoretical predictions.

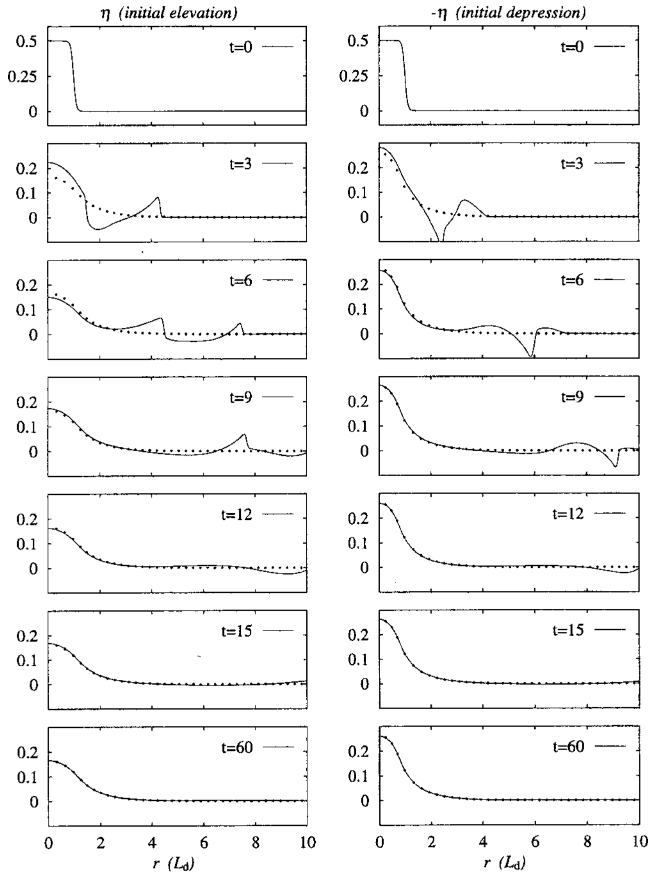

FIG. 14. Time-dependent mass adjustment: the evolution of the perturbation height field η (solid lines) for an initial height elevation (right) and depression (left) of equal initial amplitude. Note that, for the latter, $-\eta$ is plotted. The dotted lines are the end states predicted using conservation laws. $A_\eta=\pm0.5$, $R_i=1.0$, and $R_E=0.1$.

Third, as the figure shows at $t=60$, the final state fields are well predicted by the conservation methods of Sec. II and show considerable asymmetry between the initial elevation and depression. Somehow, the dissipation associated with the multiple shocks present in the flow plays a minor role, and thus conservation methods are excellent predictors of the balanced end states.

In Fig. 15 we provide some diagnostic information for the numerical experiments in Fig. 14. Consider first the perturbation height field at a specific location, $r=7$, plotted as a function of time in Fig. 15(a). This plot gives an idea of the magnitude and duration of the emitted gravity waves. Initially, the amplitudes are high, but rapidly fall off to less than ten percent of their peak value (in a time of about $15/f$). There does not seem to be a strong asymmetry (between

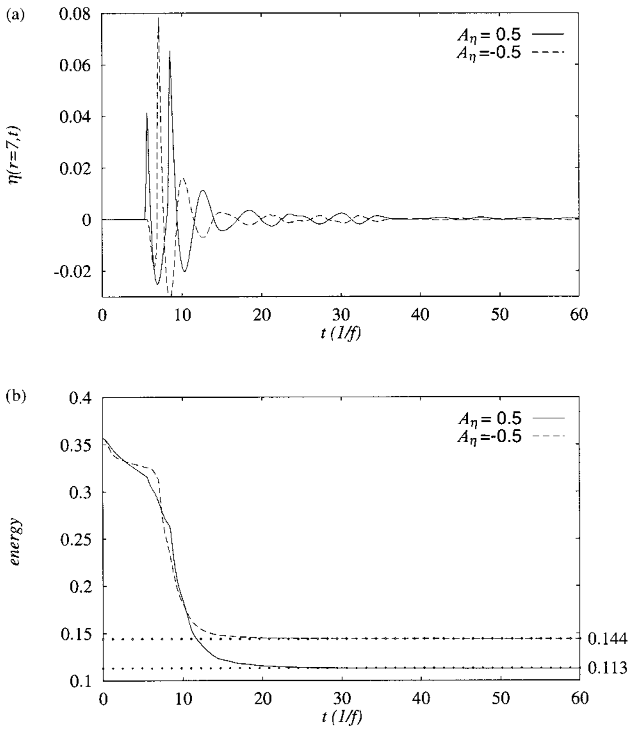

FIG. 15. Time-dependent axisymmetric mass adjustment. The (a) perturbation height field at $r=7$ and (b) the total energy in a region $x\in[-7,7]$ and $y\in[-7,7]$, as a function of time. The energy predicted in the final state is shown in dotted lines.

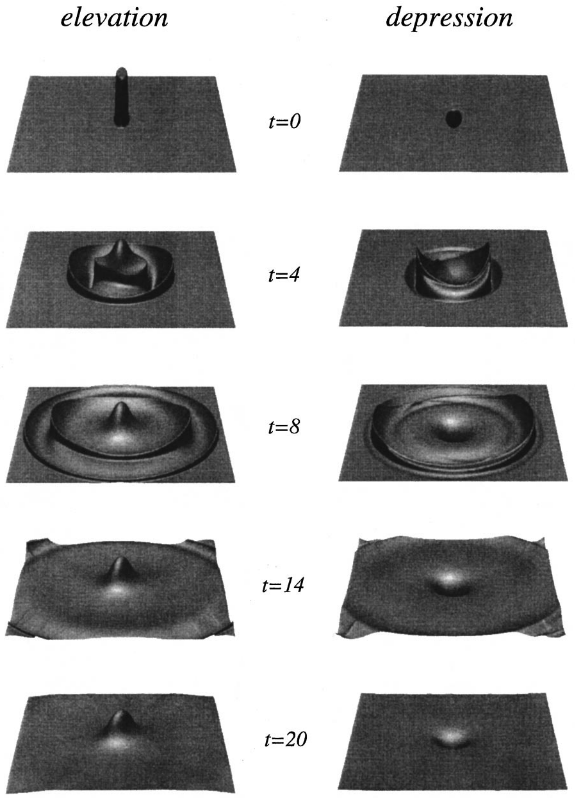

FIG. 16. Time-dependent mass adjustment: the evolution of the perturbation height field with an elliptical initial configuration, perspective view.

elevations and depressions) in the magnitude of the gravity waves that are created.

In Fig. 15(b), the total energy in the box region $x\in[-7,7]$ and $y\in[-7,7]$ is plotted as a function of time for this same adjustment scenario. The energy curves can be separated into three distinct regimes. Before $t\approx 8$, there is energy loss due to the presence of shocks (recall that if shocks were not present, the energy would remain exactly constant until the waves reach the edges of the box region). Between $t\approx 8$ and $t\approx 20$, the energy loss is due to gravity wave flux out of the box region. After $t\approx 20$, the energy equilibrates to a constant value, and the evolution is mainly governed by slow vortex/balanced dynamics.

The energy at the final adjusted state, predicted using (5), is plotted in dotted lines in Fig. 15(b). It is clear here that the theoretical predictions match well with the numerical integrations. The strongest asymmetry in the plot is evident not during the transient adjustment but at the final state: the elevation ends up losing more energy than the depression, as previously mentioned.

B. Nonaxisymmetric mass adjustment

We next examine the extent to which the above results hold for more general initial mass imbalances. The simplest nonaxisymmetric configuration is an elliptical mass imbalance. The main novelty in this case is that there need no longer be a time-independent end state since the adjustment is fully two-dimensional. Because of this fact, and the fact that material fluid parcels have the freedom to cross around one another, conservation methods such as those used in Secs. II–III cannot be applied here. The long time evolution can only be investigated through direct numerical integration.

The elliptical initial conditions we consider are again given by (12), but with the aspect ratio $\lambda\neq 1$. Our aim here is not to thoroughly investigate the entire $(A_\eta, R_i, R_E, \lambda)$ parameter space. We simply wish to bring out some general features of 2D time-dependent nonaxisymmetric adjustment, and determine whether any fundamental differences exist between this case and the axisymmetric case. Thus, we retain all parameters from the previous axisymmetric case ($A_\eta=\pm 0.5$, $R_i=1.0$, $R_E=0.1$), but increase the aspect ratio to $\lambda=2.5$. As before, the initial velocity fields are identically zero.

The resulting adjustment is shown in Fig. 16. The perturbation height field is plotted at a sequence of times, from $t=0$ to $t=20$, for both an initial elliptical height elevation (left column) and depression (right column). The ellipses are centered on each plot in the square region $x\in[-10,10]$, $y\in[-10,10]$.

At short times, the gravity wave dynamics are highly nonlinear, and the wave patterns which arise are complex. The asymmetry in the fields between elevations and depressions, and the departure from axisymmetry are obvious. As in the axisymmetric case (Fig. 14), one can see that the elliptical elevation leads to the formation of two shock waves propagating outwards, while the elliptical depression leads to a leading rarefaction wave followed by a strong shock ($t=4$). By $t=14$, in both cases, no new waves appear to be *(a) elevation*

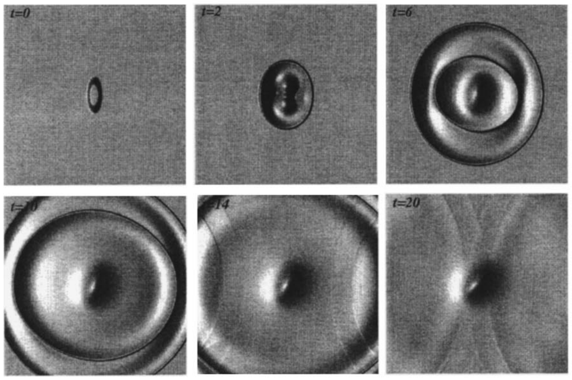

(b) depression

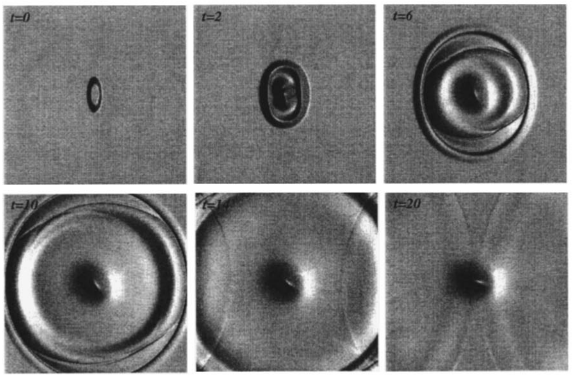

FIG. 17. Time-dependent mass adjustment: the evolution of the perturbaton height field with an elliptical initial configuration, plan view.

generated, implying that the fast wave portion of the adjustment is very nearly completed, and by $t=20$ the adjustment in the height field appears complete.

In Fig. 17, a plan view of the same numerical experiment is given. Note that the light source is situated to the left in each plot, so that an elevation is shaded to the right and a depression to the left. It should also be clear from the plots that the elevation (depression) is slowly precessing clockwise (counterclockwise). At $t=14$ and $t=20$ there is some evidence of small, nonphysical reflected waves from the boundary reentering the computational domain, but these waves have little real effect on their computed solutions since the amplitudes are small and the dynamics is linear.

Unlike the previous axisymmetric case, the potential vorticity dynamics in the nonaxisymmetric case is worth examining in some detail. We have already demonstrated that potential vorticity is rearranged during adjustment by showing how it differs between its initial and final states. However, no considerations as yet have been given to the time evolution of the potential vorticity field. By examining the evolution, it will be shown that potential vorticity can be modified on fast $(1/f)$ times scales, and that these changes persist on slow/long time scales ''irreversibly'' (in the language of Buhler and McIntyre).[26] It is therefore conjectured that gravity waves are responsible for these changes. It would then follow that nonlinear geostrophic adjustment provides one example whereby potentio-vortical dynamics can be influenced nontrivially by fast gravity waves.

In Fig. 18, we superimpose the potential vorticity contours associated with the initial height elevation (solid lines) and depression (dashed lines) for the numerical experiment shown in Fig. 17. The potential vorticity is normalized so that the maximum value in both cases is equal to one (after the background value is subtracted off); contours at levels of 0.2, 0.5, and 0.8 are then plotted. Note that the top two rows of Fig. 18 show time frames identical to those in Fig. 17. Three additional times are plotted in the bottom row, at $t=50$, 70, 90, long after the fast wave portion of the adjustment is complete.

At $t=0$, the solid potential vorticity contours associated with the elevation nearly superimpose on the dashed potential vorticity contours associated with the depression. At $t=2$, the contours associated with the depression (elevation) shrink (expand), as already noted in the axisymmetric case. By $t=6$, counterclockwise (and clockwise) precession of the potential vorticity is evident. This precession is what one would expect from considerations of slow/balanced potential vorticity dynamics alone (any elliptical vortex precesses about its centroid, e.g., a Kirchhoff vortex[27]). From the plan view of the height field (Fig. 17), it is clear that large amplitude gravity waves are present in the region of the potential vorticity contours plotted here (at least up to $t\approx 6$), and that they affect the potential vorticity evolution. Consider, for instance, how the potential vorticity is compressed/expanded on a fast time scale, between $t=0$ and $t=2$, corresponding to the net inward/outward initial wave adjustment. In view of this, the potential vorticity dynamics for $t\lesssim 6$ might more aptly be termed ''wave-influenced potential vorticity dynamics.''

At $t=20$, notice that the cyclonic vortex is precessing slightly faster than the anticyclonic one. From the study of axisymmetric mass adjustment, we can expect this, since cyclones created in this way are associated with stronger velocities and thus presumably faster rates of precession. Comparing the figure at $t=90$ with the figure at $t=2$, it appears as if the cyclonic vortex undergoes some axisymmetrization (note the hint of filamentary tails at $t=70$). The anticyclonic vortex, on the other hand, seems to retain its $t=2$ elliptical shape rather well.

Finally, for completeness, we plot in Fig. 19 pointwise height and energy measures analogous to those for the axisymmetric case in Fig. 15. The (a) pointwise value of η evaluated at $x=7$, $y=0$, and (b) the energy in a box region $x\in[-7,7]$, $y\in[-7,7]$, both demonstrate that the time required for adjustment to complete is *not* strongly dependent on the aspect ratio of the initial mass imbalance. In the elliptical case, the adjustment takes about 15–20 $(1/f)$ to complete, as in the axisymmetric case. The main difference between the two cases is seen at long times: the energy of the elliptical vortices at $t=60$ (dotted lines) is less than for their axisymmetric counterparts. Note that, in both cases, more energy is lost to gravity waves during the generation of anticyclones (solid lines).

VI. SUMMARY AND DISCUSSION

In this article we have revisited the classic problem of geostrophic adjustment and have shown how it can be re-

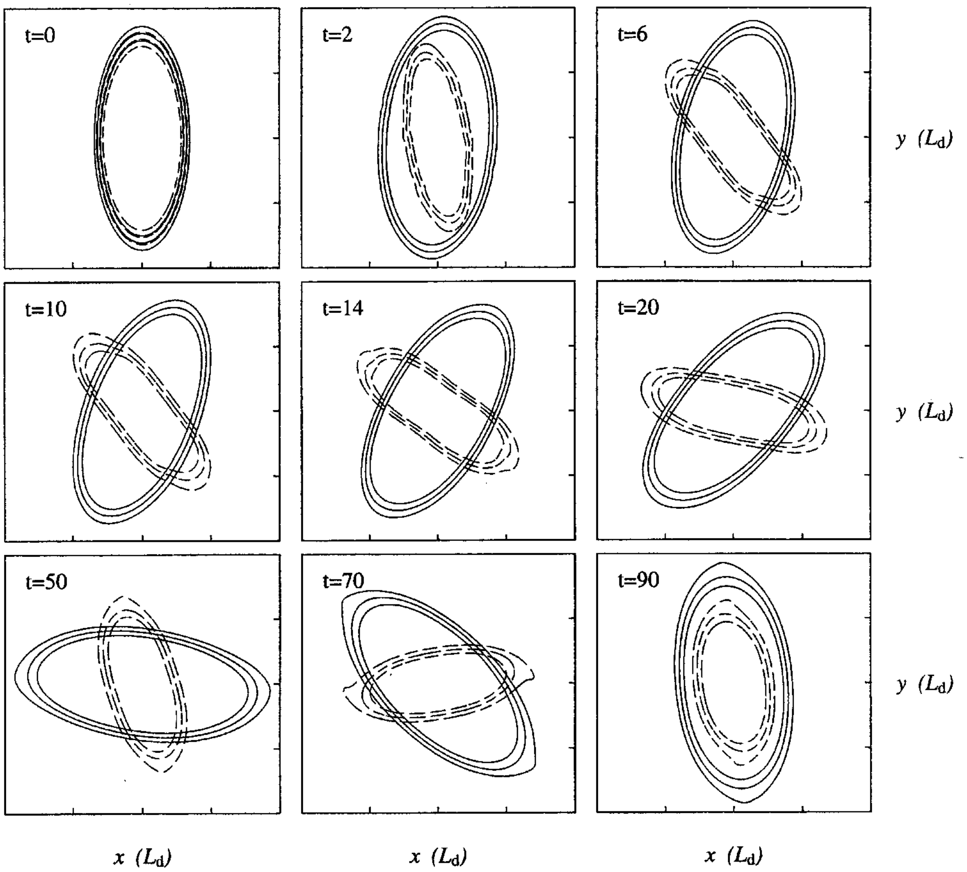

FIG. 18. The potential vorticity for the nonaxisymmetric adjustment shown in Fig. 17. The potential vorticity associated with the height elevation (final state anticyclone) is plotted in solid lines, while the potential vorticity for the height depression (final state cyclone) is plotted in dashed lines.

sponsible for the creation cyclone/anticyclone asymmetry. Such asymmetry spontaneously appears in *f*-plane shallow-water turbulence simulations,[13,14,28] and has been studied in a variety of contexts.[15,29,30] It would seem worthwhile, therefore, to attempt to draw from the results discussed in this article some general conclusions regarding this asymmetry and to relate those conclusions to previous work.

We have found that, in the context of an *f*-plane shallow-water model, the degree of asymmetry in the final state during mass and momentum adjustment is directly proportional to the amount of initial imbalance, and that the asymmetry reaches a local maximum for imbalances of deformation radius scale. The adjustment of equal and opposite axisymmetric *mass* imbalances leads to the formation of balanced cyclones that are stronger than the corresponding anticyclones. Furthermore, the formation of these balanced cyclones is associated with comparatively weaker gravity wave energy flux. In contrast, with the exception of anomalous cases, the adjustment of equal and opposite axisymmetric *momentum* imbalances leads to balanced cyclones that are weaker than the corresponding anticyclones. In that case, the formation of balanced cyclones is associated with a stronger gravity waves energy flux for the reader who may be wondering whether geometrical effects are crucial to these result, we note that an identical analysis has been carried out[9] using rectilinear configurations and that the qualitative results are identical to the axisymmetric results shown here.

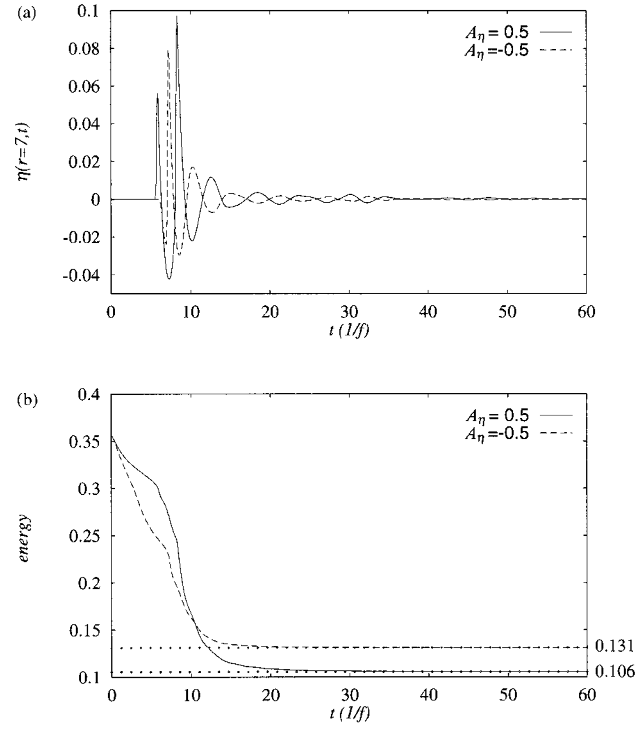

FIG. 19. Time-dependent elliptical mass adjustment. The (a) perturbation height field at $x=7$, $y=0$ and (b) the total energy in a region $x\in[-7,7]$ and $y\in[-7,7]$, as a function of time. The energy at the final states (empirically defined at $t=60$) is shown in dotted lines.

The fact that the relative strength of the vortices created during adjustment depends strongly on the type of initial imbalance (mass or momentum) makes it difficult to use these results to directly explain the observed asymmetry in the above mentioned turbulence simulations. Recall that, in those simulations, strong cyclone/anticyclone asymmetry is found in those parametric regimes where balance is likely to break down, in which case adjustment would occur. For such adjustment, however, both mass and momentum fields are initially present, and this prevents us from directly applying our results to those simulations.

Finally we note that another motivation for this work, besides its importance in understanding the geostrophic adjustment process, is to explore nontrivial ways by which gravity waves can affect balanced flows, i.e., large-scale atmospheric and oceanic flows which are governed by the notion of potential vorticity invertibility (the reader is referred to Ford[31] for a review of this concept and some of its limitations; see also Refs. 32 and 33). For instance, Buhler and McIntyre[26] have recently shown how gravity waves may be able to modify an exactly balanced flow in a β-channel irreversibly via resonant instability. Here, ''irreversible'' modification was taken in the sense of lasting deformation of potential vorticity contours as a direct result of the passage of gravity waves through the balanced flow.

In this article we have shown how the adjustment process too can lead to lasting deformation of potential vorticity contours and we have argued that the gravity waves generated during adjustment are responsible for these changes. Thus, even though the flows we have considered are not initially balanced, one may consider geostrophic adjustment to be a mechanism for irreversible potential vorticity change. Of course, the degree to which the potential vorticity changes depends on the amount of initial imbalance. The question then is: how much initial imbalance is needed to produce a sizeable effect on the potential vorticity? As we have demonstrated in Sec. IV above (cf. Fig. 13), for a modest initial depression with $|A_\eta| = 0.3$, which can be interpreted as the maximum advective Rossby number during the time-dependent adjustment process, roughly 20% changes in the potential vorticity distribution are possible.

ACKNOWLEDGMENTS

We would like to thank Oliver Buhler and Rupert Ford for helpful discussions, and the National Science Foundation for its support.

[1] C. G. Rossby,''On the mutual adjustment of pressure and velocity distributions in certain simple current systems II,'' J. Mar. Res. **1**, 239 (1938).

[2] A. Cahn,''An investigation of the free oscillations of a simple current system,'' J. Met. **2**, 113 (1945).

[3] A. M. Obukhov,''On the question of the geostrophic wind,'' Izv. Akad. Nauk SSSR, Ser. Geogr. Geofiz. **13**, 281 (1949).

[4] B. Bolin,''The adjustment of a non-balanced velocity field toward geostrophic equilibrium in a stratified fluid,'' Tellus **5**, 373 (1953).

[5] G. Veronis,''Partition of energy between geostrophic and non-geostrophic oceanic motions,'' Deep-Sea Res. **3**, 157 (1956).

[6] W. Blumen,''On nonlinear geostrophic adjustment,'' Rev. Geophys. Space Phys. **24**, 325 (1967).

[7] W. Blumen,''Geostrophic adjustment,'' Rev. Geophys. Space Phys. **10**, 485 (1972).

[8] A. E. Gill,''Adjustment under gravity in a rotating channel,'' J. Fluid Mech. **103**, 275 (1976).

[9] A. C. Kuo, ''Geostrophic adjustment and wave-vortex interaction in rotating shallow water,'' Ph.D. thesis, Columbia University, 1999.

[10] J. C. McWilliams,''Sub-mesoscale coherent vortices in the oceans,'' Rev. Geophys. **23**, 165 (1985).

[11] H. B. Bluestein, *Synoptic-Dynamic Meteorology in Midlatitudes. Vol. II. Observations and Theory of Weather Systems* (Oxford University Press, New York, 1993).

[12] M-M. MacLow and A. P. Ingersoll,''Merging of vortices in the atmosphere of Jupiter: an analysis of voyager images,'' Icarus **65**, 353 (1986).

[13] L. M. Polvani, J. C. McWilliams, M. A. Spall, and R. Ford,''The coherent structures of shallow water turbulence: deformation radius effects, cyclone/anticyclone asymmetry and gravity wave generation,'' Chaos **4**, 177 (1994).

[14] M. Arai and T. Yamagata,''Asymmetric evolution of eddies in rotating shallow water,'' Chaos **4**, 163 (1994).

[15] I. Yavneh, A. F. Shchepetkin, J. C. McWilliams, and L. P Graves,''Multigrid solution of rotating, stably stratified flows: The balance equations and their turbulent dynamics,'' J. Comput. Phys. **136**, 245 (1997).

[16] V. D. Larichev and J. C. McWilliams,''Weakly decaying turbulence in an equivalent barotropic model,'' Phys. Fluids A **3**, 938 (1991).

[17] J. Pedlosky, *Geophysical Fluid Dynamics* (Springer-Verlag, New York, 1987).

[18] E. Boss and L. Thompson,''Energetics of nonlinear geostrophic adjustment,'' J. Phys. Oceanogr. **25**, 1521 (1995).

[19] J. R. Holton, Jr., *An Introduction to Dynamic Meteorology* (Academic, New York, 1979).

[20] W. H. Schubert, J. J. Hack, P. L. Silva Dias, and S. R. Fulton,''Geostrophic adjustment in an axisymmetric vortex,'' J. Atmos. Sci. **37**, 1464 (1980).

[21] J. C. McWilliams,''Vortex generation through balanced adjustment,'' J. Phys. Oceanogr. **18**, 1178 (1988).

[22] M.-P. Lelong and J. C. McWilliams, ''Cyclostrophic adjustment in shallow water and Boussinesq fluids,'' J. Fluid. Mech. (submitted).

[23] A. C. Kuo and L. M. Polvani,''Time-dependent fully nonlinear geostrophic adjustment,'' J. Phys. Oceanogr. **27**, 1614 (1997).

[24] G. S. Jiang and C. W. Shu,''Efficient implementation of weighted ENO schemes,'' J. Comput. Phys. **126**, 1351 (1996).

[25] A. Sommerfeld, *Lectures on Theoretical Physics, Vol. 3: Electrodynamics* (Academic, New York, 1964).

[26] O. Buhler and M. E. Mcintyre,''On non-dissipative wave-mean interactions in the atmosphere or oceans'', J. Fluid Mech. **354**, 301 (1998).

[27] H. Lamb, *Hydrodynamics* (Dover, New York, 1945).

[28] I. Yavneh and J. C. McWilliams,''Breakdown of the Slow Manifold in the shallow-water equations,'' Geophys. Astrophys. Fluid Dyn. **75**, 131 (1994).

[29] B. Cushman-Roisin and B. Tang,''Geostrophic turbulence and emergence of eddies beyond the radius of deformation,'' J. Phys. Oceanogr. **20**, 97 (1990).

[30] M. V. Nezlin and E. N. Snezhkin, *Rossby vortices, spiral structures, solitons: astrophysics and plasma physics in shallow water experiments* (Springer-Verlag, Berlin, 1993).

[31] R. Ford, ''Gravity wave generation by vortical flows in a rotating frame,'' Ph.D. thesis, Cambridge University, 1993.

[32] M. E. McIntyre and W. A. Norton, ''Potential-vorticity inversion on a hemisphere,'' J. Atmos. Sci., in press (2000).

[33] R. Ford, W. A. Norton, and M. E. Mcintyre, ''Balance and the slow quasimanifold: some explicit results,'' J. Atmos. Sci., in press (2000).